Nanoscale

PAPER

View Article Online
View Journal | View Issue



Cite this: *Nanoscale*, 2025, **17**, 5090

# Built-in electric field in the Mn/$C_{60}$ heterojunction promotes electrocatalytic nitrogen reduction to ammonia†

Hao Xue,[a,b] Kaiheng Zhao,[c] Denglei Gao,[d] Fangying Duan,[e] Zijian Gao,[f] Wenjia Yu,[g] Sha Li,*[h] Menglei Yuan*[b,e] and Zongjing Lu*[a]

The electrochemical nitrogen reduction reaction (NRR) has been regarded as a green and promising alternative to the traditional Haber–Bosch process. However, the high bond energy (940.95 kJ $mol^{-1}$) of the N≡N triple bond hinders the adsorption and activation of $N_2$ molecules, which is a critical factor restricting the catalytic performance of catalysts and their large-scale applications. Herein, an Mn/$C_{60}$ heterostructure is constructed *via* a simple grinding and calcination process and achieves an extraordinary faradaic efficiency of 42.18% and an $NH_3$ yield rate of 14.52 μg $h^{-1}$ $mg_{cat}^{-1}$ at −0.4 V *vs.* RHE in 0.08 M $Na_2HPO_4$. Our experimental and theoretical results solidly confirm that the spontaneous charge transfer at the Mn/$C_{60}$ heterointerface promotes the formation of a built-in electric field, which facilitates the electron transfer from Mn towards $C_{60}$ and creates localized electrophilic and nucleophilic regions. The formation of the space-charge region effectively optimized the adsorption energy of the key intermediate *NH–*$NH_2$ and also reduced the free energy barrier for the hydrogenation step of *NH–*NH to *NH–*$NH_2$. Furthermore, the calculated lower limiting potential ($U_{L(NRR)}$) in Mn/$C_{60}$ relative to the HER ($U_{L(HER)}$) demonstrates its enhanced selectivity toward the NRR. This work provided new insights into enhancing the activity and performance of electrocatalysts for the NRR by constructing heterojunctions to improve nitrogen adsorption.

Received 29th October 2024,
Accepted 2nd January 2025

DOI: 10.1039/d4nr04496g

rsc.li/nanoscale



## Introduction

Ammonia ($NH_3$) is indispensable in agriculture and industry, enabling large-scale fertilizer production and supporting various chemical processes.[1–3] Its high hydrogen concentration and carbon-free nature position it as a promising energy carrier for sustainable energy solutions and climate mitigation.[4,5] The large-scale synthesis of $NH_3$, initiated by the Haber–Bosch process in the early 20th century, is thermodynamically exothermic and spontaneous ($N_2(g) + 3H_2(g) \rightarrow 2NH_3(g)$, $\Delta_r H_m^\theta$ = −92.22 kJ $mol^{-1}$, and $\Delta_r G_m^\theta$ = −32.90 kJ $mol^{-1}$). This reaction requires high temperature (350 °C–450 °C) to accelerate the reaction rate due to the strong bond energies of the N≡N triple bond (940.95 kJ $mol^{-1}$), and the substantial energy barrier (410 kJ $mol^{-1}$) in the first step of N≡N triple bond dissociation and high pressure (100–200 bar) to ensure a forward reaction according to Le Chatelier's principle.[5–8] However, the Haber–Bosch process not only leads to significant energy costs but also generates large amounts of greenhouse gases (mainly $CO_2$) during the steam methane reformation (SMR) process to produce $H_2$.[9] Recently, the electrocatalytic nitrogen reduction reaction (NRR) powered by renewable energy sources, such as wind and solar, in aqueous electrolytes presents a promising alternative to the Haber–Bosch process for efficient $NH_3$ synthesis.[10–13] Nevertheless, the performance of NRR electrocatalysts remains insufficient to meet the requirements for practical applications.[14,15]

Encouragingly, designing a heterogeneous interface to construct a built-in electric field is considered an effective strategy for enhancing electrocatalytic activity, which accelerates the

[a]*Institute of Photochemistry and Photofunctional Materials, University of Shanghai for Science and Technology, Shanghai 200093, China. E-mail: zongjinglu@usst.edu.cn*
[b]*Queen Mary University of London Engineering School, Northwestern Polytechnical University, Xi'an 710129, China*
[c]*Key Laboratory of Photochemistry, Institute of Chemistry, Chinese Academy of Sciences, University of Chinese Academy of Sciences, Beijing 100190, China*
[d]*School of Chemical Engineering, Shandong Institute of Petroleum and Chemical Technology, Dongying 257061, China*
[e]*State Key Laboratory of Solidification Processing and School of Materials Science and Engineering, Northwestern Polytechnical University, Xi'an 710072, China. E-mail: mlyuan@nwpu.edu.cn*
[f]*CAS Key Laboratory of Green Process Engineering, Institute of Process Engineering, Chinese Academy of Sciences, Beijing 100190, China*
[g]*Yantai Research Institute of Harbin Engineering University, Yantai 264006, China*
[h]*Chemistry and Chemical Engineering Guangdong Laboratory, Shantou 515021, China. E-mail: lisha@ccelab.com.cn*

†Electronic supplementary information (ESI) available. See DOI: https://doi.org/10.1039/d4nr04496g

reaction kinetics by promoting electron transfer and reactant diffusion.[16] In general, to construct the built-in electric field, at least one of the two heterojunction components should be a semiconductor. The work function difference between the two materials of a heterojunction induces interfacial polarization, generating a potential difference that promotes the spontaneous movement of electrons near the interface until the Fermi level on two sides is balanced, which ultimately forms localized electron-rich and electron-deficient regions, creating a charge distribution gradient and establishing a built-in electric field.[16,17] This built-in electric field facilitates electron transfer and modulates the charge density around active sites, thereby enhancing the intrinsic activity of the electrocatalyst. According to the types of the two materials, the heterojunction could be categorized as: (i) p–n heterojunction, (ii) p–p heterojunction, (iii) n–n heterojunction, and (iv) Mott–Schottky heterojunction. The Mott–Schottky heterojunction is a metal–semiconductor interface formed when a metal comes into close contact with a semiconductor that possesses a different Fermi level than that of the metal. For example, if a metal is in contact with a p-type semiconductor (which has electron holes as majority carriers), the electrons in the metal region will flow towards the p-type semiconductor due to the work function difference, which ultimately constructs a built-in electric field from the metal to the semiconductor. A variety of transition metals (TMs), such as Fe,[18,19] Ru,[20,21] and Mo,[22] have demonstrated excellent NRR activity due to their favorable combination of occupied and unoccupied d orbitals, which possesses suitable energy and symmetry for σ donation from the occupied σ orbital of $N_2$ to the empty orbital of the metal atom and π back-donation from the occupied orbital of the metal atom to the empty π* orbital of $N_2$.[23,24] Ludden *et al.* indicated that Mn element is capable of improving the catalytic activity of nitrogenases extracted from the photosynthetic bacterium *Rhodospirillum rubrum*.[25] Mn has 3d orbitals with appropriate energy and symmetry, enabling it to achieve the aforementioned donation and back-donation effects, which are beneficial for the adsorption and activation of $N_2$ molecules.[2,26–28] However, the unoccupied d orbitals in the metal may lead to the formation of strong metal–H bonds, which kinetically enhance the unfavorable competitive hydrogen evolution reaction (HER), causing a relatively poor selectivity towards the NRR.[23,29] Recent studies have demonstrated that tuning the electronic structure around Mn can effectively enhance its NRR activity and selectivity.[26,28,30,31] Du and colleagues proposed a band structure regulation strategy through alloying, which helps to mitigate the HER issue of Mn.[32] The constructed MnP alloy showed a reduced HOMO energy level compared to Mn and suppressed HER behavior. Buckminsterfullerene ($C_{60}$) has a closed cage-like structure composed of hexagons with alternating single and double bonds and pentagons connected by single bonds,[33] which not only provides a curved surface but also exhibits unique electron-withdrawing properties to work as an excellent electron acceptor.[34,35] Its narrow bandgap (approximately 1.6–1.9 eV) makes it an excellent semiconductor material for the construction of Mott–Schottky heterojunctions.[36–38] Moreover, a series of theoretical and experimental studies have demonstrated the pronounced electron-withdrawing capability of $C_{60}$, underscoring its potential to effectively mitigate the competitive HER at metal active sites while facilitating the NRR.[39–41] Therefore, exploring the strategy of constructing a Mn/$C_{60}$ Mott–Schottky heterojunction for the NRR holds great promise. However, no such studies have been reported to date.

In this work, a simple grinding and calcination process was utilized to synthesise and construct an Mn/$C_{60}$ heterostructure with the purpose of forming a built-in electric field, which was advantageous for accelerating charge transfer and optimizing

**Menglei Yuan**

*Menglei Yuan is an associate professor in the School of Materials Science and Engineering, Northwestern Polytechnical University. He received his bachelor's degree in engineering from the North University of China in 2017. In the same year, he went to the Institute of Process Engineering, Chinese Academy of Sciences, for direct doctoral training. He joined the Northwestern Polytechnical University in 2022. Currently, he focuses on electrocatalytic small molecule activation and organic electrosynthesis reactions for the preparation of high-value chemicals such as ammonia, urea, amides, olefins,* etc. *He mainly focuses on two aspects, namely electrocatalyst design and regulation and electrolyte coupling enhancement.*

**Zongjing Lu**

*Zongjing Lu received his Ph.D. in applied chemistry from Tianjin University, China, under the supervision of Prof. Jiannian Yao. He subsequently joined the University of Shanghai for Science and Technology in November 2023 as an assistant professor and established his research group. His current research interests mainly focus on the development of new catalytic materials for catalysis-related applications, such as electrolytic nitrogen/nitrate reduction, plastic decomposition, biomass conversion, and the in-depth understanding of catalytic mechanisms.*

the Gibbs free energy for intermediate adsorption. The built-in electric field could promote electron transfer and tune the charge density around active Mn sites to suppress the competitive HER and reduce the energy barriers of the NRR. Therefore, the fabricated $Mn/C_{60}$ catalyst achieved a remarkable faradaic efficiency of 42.18% and an $NH_3$ yield rate of 14.52 μg $h^{-1}$ $mg_{cat}^{-1}$ at −0.4 V *vs.* RHE. This work aimed to achieve efficient electrochemical ammonia synthesis at ambient temperature and pressure through exploring the strategy of constructing an $Mn/C_{60}$ heterostructure.

## Results and discussion

The $Mn/C_{60}$ catalyst was synthesized *via* a simple grinding and low-temperature (300 °C) annealing process. As shown in Fig. 1a, the X-ray diffraction (XRD) patterns of the prepared $Mn/C_{60}$ catalyst exhibit pronounced characteristic $C_{60}$ peaks and recognizable peaks of Mn. The peaks at 10.8°, 17.7°, 20.8°, 21.7°, 27.4°, 28.2°, 30.9°, 32.8°,42.2° and 48.1° were indexed to the (111), (220), (311), (222), (331), (420), (422), and (511) planes of $C_{60}$ and the (101) and (110) planes of Mn, respectively. The other peaks in the XRD graph may be attributed to $MnO_x$ generated from the oxidation of Mn element.[42] The corresponding morphology of the catalyst, as revealed by the scanning electron microscopy (SEM) image (Fig. 1b and c), demonstrated that an abundant amount of nanoparticles with small particle sizes (an average diameter of approximately 0.18 μm) (Fig. S1†) were highly dispersed on the substrate. Furthermore, the high resolution transmission electron microscopy (HRTEM) image of $Mn/C_{60}$ further validated that Mn nanoparticles were well dispersed on the $C_{60}$ substrate (Fig. 1d and e). In the HRTEM image of $Mn/C_{60}$ (Fig. 1f), the well-resolved lattice fringes of 2.14 nm corresponded to the (101) lattice of Mn. Similarly, the HRTEM image of the substrate exhibited interplanar distances of 2.72 nm and 3.16 nm, which could be ascribed to the (511) and (420) planes of $C_{60}$, indicating the successful preparation of $Mn/C_{60}$, consistent with the SEM observations. Due to the low concentration of Mn, high-angle annular dark-field scanning transmission electron microscopy (HAADF-STEM) (Fig. 1g) and the corresponding energy dispersive spectroscopy (EDS) were employed to precisely identify the spatial distribution and elemental composition of Mn on the $C_{60}$ substrate. The EDS elemental mapping images of C (Fig. 1h) and Mn (Fig. 1i) elements in the $Mn/C_{60}$ catalyst show that Mn was uniformly dispersed across the $C_{60}$ substrate in the form of nanoparticles. Combined with the weak Mn characteristic peaks in the XRD pattern, the high dispersion of Mn on the $C_{60}$ substrate was further confirmed, establishing a critical foundation for the strong electronic interactions between Mn and $C_{60}$. Moreover, the well-defined lattice fringe distribution was indicative of the heterogeneous structure formed between Mn and $C_{60}$, facilitating the formation of an intrinsic built-in electric field.

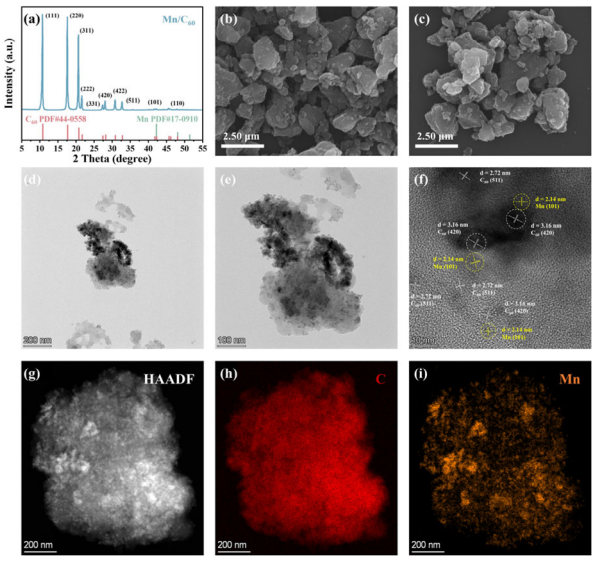


**Fig. 1** (a) Experimental XRD patterns of the as-prepared $Mn/C_{60}$; (b and c) SEM image of the $Mn/C_{60}$ catalyst; (d–f) high-magnification TEM image of $Mn/C_{60}$; (g–i) the corresponding energy-dispersive X-ray spectroscopy (EDS) elemental mapping of $Mn/C_{60}$.

Based on the results obtained from the aforementioned characterization techniques, we successfully demonstrated the construction of the $Mn/C_{60}$ heterostructure. Subsequently, it was imperative to confirm the presence of the built-in electric field and examine the charge distribution around Mn and $C_{60}$ through a combination of theoretical calculations and experimental characterization. First, based on the crystallographic information observed from XRD and TEM, we modeled the Mn (101) crystal plane and $C_{60}$ and computed their work functions, respectively. The work function of the Mn (101) crystal plane was found to be 3.75 eV, while that of $C_{60}$ was 5.52 eV, confirming that the two materials met the necessary conditions for the formation of a built-in electric field, specifically, an appropriate work function difference ($\Delta\Phi$ = 1.77 eV) (Table S1†). The work function difference between the two materials drove directional electron transfer at the interface, aligning the Fermi levels on both sides. Further differential charge density and Bader charge analysis (Fig. 2a and b) confirmed the spontaneous electron transfer from Mn to $C_{60}$ (1.10 $e^-$), which was consistent with the results observed in X-ray photoelectron spectroscopy (XPS). The corresponding charge accumulation and depletion generated locally electrophilic Mn sites and nucleophilic $C_{60}$ sites, optimizing the adsorption of the reactant/intermediate during the NRR through electrostatic interactions.

X-ray photoelectron spectroscopy (XPS) was performed to further elucidate the chemical composition and variations in the elemental valence state of the synthesized $Mn/C_{60}$ catalyst. The significant signals for C, O, and Mn could be observed in the survey spectra (Fig. 3a). More specifically, in the high-resolution C 1s spectra (Fig. 3b), the highest characteristic peak at 284.75 eV corresponds to the C–C/C=C bond and the other three weak peaks at 286.49 eV, 288.67 eV and 290.54 eV could be attributed to the C–O bond, C=O bond and π–π* sat-

 

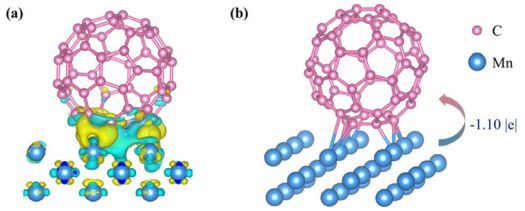


**Fig. 2** (a) Charge density difference of the $Mn/C_{60}$ heterojunction; yellow and cyan indicate electron accumulation and depletion, respectively, with isosurface values of 0.009 e $Å^{-3}$. (b) Bader charge analysis for $Mn/C_{60}$. Colour code: pink, C; blue, Mn.

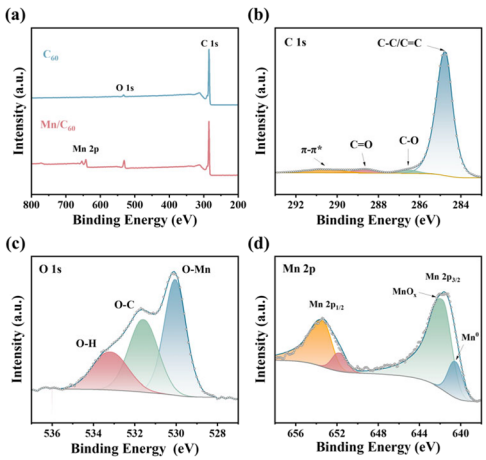


**Fig. 3** (a) XPS survey spectrum of $Mn/C_{60}$, and high-resolution XPS spectra of (b) C 1s, (c) O 1s, and (d) Mn 2p.

ellite, respectively. Meanwhile, in the high-resolution O 1s spectra (Fig. 3c), the three peaks at 530.05 eV, 533.16 eV and 531.58 eV could be attributed to the O–Mn, O–H, and O–C bonds, stemming from inevitable metal surface oxidation, surface-adsorbed water and oxygen, respectively.[43] Intriguingly, in the high-resolution Mn 2p spectra, the $Mn^0$ $2p_{3/2}$ peaks depicted a shift towards higher binding energies (Fig. 3d) compared with the characteristic peak of pristine Mn nanoparticles (639.0 eV),[43,44] indicating strong electronic interactions between Mn and $C_{60}$. More concretely, the positive shift of $Mn^0$ $2p_{3/2}$ peaks implied an increased oxidation state of Mn, which could be ascribed to the charge transfer from Mn to $C_{60}$. The aforementioned results indicated the successful construction of the $Mn/C_{60}$ heterostructure and effective charge transfer between Mn and $C_{60}$, resulting in the formation of localized electrophilic and nucleophilic regions.[17,45] This local charge redistribution established a built-in electric field that optimized the adsorption of the reactant/intermediate, thereby improving the performance of the electrocatalytic NRR.

The NRR measurements were carried out with a typical three-electrode system in an $N_2$-saturated 0.08 M $Na_2HPO_4$ solution utilizing a single-chamber electrolytic cell. A graphite rod, an Ag/AgCl electrode (filled with saturated KCl solution), and a piece of pretreated carbon cloth (1 × 1 $cm^2$) (with a catalyst loading of 0.3 mg) were used as the counter electrode, reference electrode, and working electrode, respectively. Note that all potentials were reported on the reversible hydrogen electrode (RHE) scale in this work. The linear sweep voltammetry (LSV) curves were first recorded in Ar-saturated and $N_2$-saturated solutions to indicate the electrocatalytic synthesis of ammonia. As shown in Fig. 4a, the current intensity in the Ar-saturated solution was smaller than that in the $N_2$-saturated solution, exhibiting an extra current density contribution from the NRR. The time-dependent chronoamperometry (CA) test was subsequently performed within the potential range of −0.2 V to −1.0 V *vs.* RHE to further quantitatively assess the electrocatalytic NRR performance of the $Mn/C_{60}$ catalyst. Fig. 4b displays all the chronoamperometric curves recorded for 1 h at various potentials in $N_2$-saturated solution with stable current densities. Obviously, the current density of $Mn/C_{60}$ increased with the applied potential. The employed ultraviolet-visible (UV-vis) absorption spectra of electrolytes based on the indophenol blue method demonstrated the largest absorption intensity (Fig. 4c) at −0.4 V *vs.* RHE after electrolysis for 1 h. Quantitatively, the $NH_3$ yields and associated FEs from the NRR were evaluated utilizing a concentration–absorbance calibration curve constructed *via* the indophenol blue method (Fig. 4d and e). The corresponding highest $NH_3$ yield rate achieved was 14.52 μg $h^{-1}$ $mg_{cat}^{-1}$ with an FE of 42.18% at −0.4 V (Fig. 4f), outperforming most of the recently reported catalysts, including Pd/C,[46] $Mn_3O_4$ nanocube[47] and C-doped $TiO_2$ nanoparticles[48] (Fig. 4g). However, the electrocatalytic NRR performance decreased when the potential becomes more negative than −0.4 V, which can be ascribed to the enhancement of the competitive HER.[49–51]

In order to show that the detected $NH_3$ was obtained from $N_2$ by the electrocatalytic NRR on the $Mn/C_{60}$ catalyst, a series of control experiments were carried out under the following conditions: (i) Ar as the feed gas and $C_{60}$/Mn as the NRR catalyst, (ii) $N_2$ as the feed gas and $C_{60}$ as the NRR catalyst, (iii) $N_2$ as the feed gas and Mn as the NRR catalyst, and (iv) $N_2$ as the feed gas and $Mn/C_{60}$ as the NRR catalyst (Fig. 4h). In addition, $^{15}N_2$ isotope labeling experiments were carried out to further exclude possible interference from any contaminants (such as adventitious $NH_3$ and $NO_X$). As shown in Fig. 4i, the triplet coupling of $^{14}NH_4^+$ and the doublet coupling of $^{15}NH_4^+$ of the standard samples can be detected in $^1H$ NMR. Only $^{15}NH_4^+$ was detected when utilizing $^{15}N_2$ as the feed gas for the NRR, which illustrated that $NH_3$ was produced by the electroreduction of $N_2$. All of these aforementioned results further confirmed that the synthesized $NH_3$ here originated from the directly supplied nitrogen during the electrocatalytic NRR instead of from other contaminants or decomposition of catalysts. Subsequently, the corresponding $NH_3$ yield and FE after electrolysis for 1 h at −0.4 V *vs.* RHE utilizing $N_2$ as the feed gas and $Mn/C_{60}$ as the NRR catalyst were much higher than those obtained utilizing $C_{60}$ or Mn as the NRR catalyst, respectively (Fig. 4j), corroborating that the electrocatalytic NRR performance was enhanced by the local charge redistribution in the $Mn/C_{60}$ heterojunction.

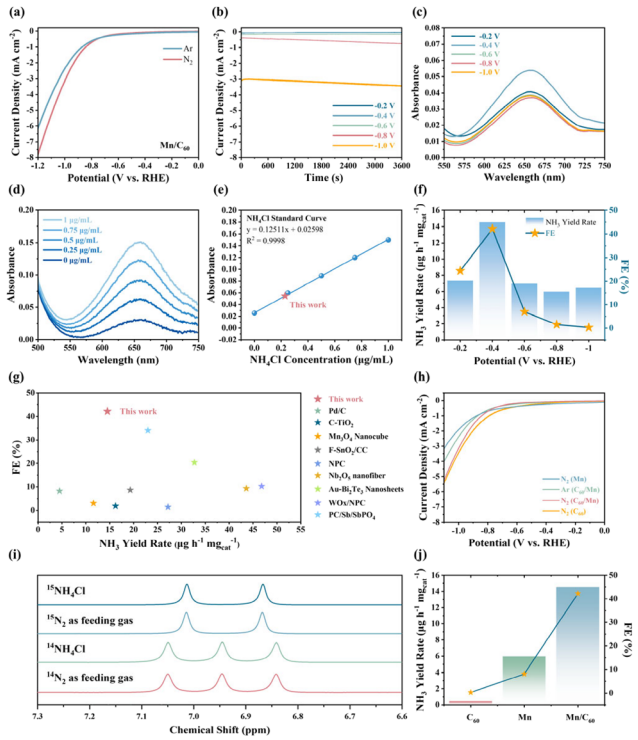

**Fig. 4** (a) Linear sweep voltammetry (LSV) of $Mn/C_{60}$ in $N_2$-saturated (red line) and Ar-saturated (blue line) 0.08 M $Na_2HPO_4$ electrolytes at 10 mV $s^{-1}$. (b) the chronoamperometric curves of $Mn/C_{60}$ in the $N_2$-saturated 0.08 M $Na_2HPO_4$ electrolyte at various potentials (−0.2 V, −0.4 V, −0.6 V, −0.8 V and −1.0 V) for 1 h. (c) UV-vis absorption spectra of the electrolytes colored with the indophenol indicator for 2 h. (d and e) Concentration–absorbance of $NH_4Cl$ solution with a series of standard concentrations (0–1.0 μg $mL^{-1}$) in 0.08 M $Na_2HPO_4$. (f) The corresponding $NH_3$ yield rate and faradaic efficiency at each given potential. (g) Comparison of the $NH_3$ yield rate and faradaic efficiency of $Mn/C_{60}$ with selected reported NRR electrocatalysts. (h) LSV curves under different conditions. (i) $^1H$ NMR spectra (700 MHz) for $^{14}NH_4^+$ and $^{15}NH_4^+$ produced from $N_2$ electrochemical reduction using $N_2$ and $^{15}N_2$ as the feeding gas, respectively. (j) Electrochemical performance of $Mn/C_{60}$, Mn and $C_{60}$.

To further explore the intrinsic reasons behind the enhanced NRR activity of $Mn/C_{60}$, DFT calculations were first performed to investigate the adsorption of $*N_2$ on pristine $C_{60}$, Mn, and $Mn/C_{60}$. For pristine $C_{60}$, a relatively high positive free energy barrier (0.49 eV) for $*N_2$ adsorption was observed (Fig. 5a), suggesting that nitrogen molecules encountered significant difficulty in adsorbing onto $C_{60}$, which aligned with the suboptimal NRR performance of pristine $C_{60}$, as shown in Fig. 4j. In contrast, as anticipated, pristine Mn exhibited excellent $N_2$ adsorption capability with a thermodynamically spontaneous $*N_2$ adsorption process (Fig. 5b). This property was also observed in $Mn/C_{60}$, presenting a spontaneously downhill step with a negative energy barrier for $*N_2$ adsorption (Fig. 5c). Additionally, an ideal NRR catalyst must carefully consider the competing HER, involving both the adsorption energies and the limiting potentials of the HER and NRR, the latter of which is discussed further in the following sections. Regarding the discussion of adsorption energies, a lower $*N_2$ adsorption energy is typically required compared to that of *H. DFT calculations revealed the adsorption energies of $*N_2$ and *H on $Mn/C_{60}$ to be −1.23 and −0.60 eV, respectively, indicating that the constructed $Mn/C_{60}$ heterostructure was energetically favored to adsorb $N_2$ rather than competitively adsorb *H (Fig. 5e). However, pristine Mn also exhibited good selectivity in the competitive adsorption of $*N_2$ and *H ($\Delta G_{*N_2} - \Delta G_{*H} = -0.95$ eV < 0) (Fig. 5b and d). Therefore, it was necessary to further investigate the reasons behind the enhanced NRR performance of $Mn/C_{60}$ compared to Mn. Subsequently, to further elucidate the impact of introducing $C_{60}$ on the NRR activity of Mn, we performed electrochemical impedance spectroscopy (EIS) measurements to investigate the influence of $C_{60}$ on the charge transfer kinetics of the Mn catalyst. The charge-transfer resistance ($R_{ct}$) of the catalyst was investigated by EIS. Nyquist plots for $Mn/C_{60}$ in Fig. 5f demonstrated a smaller semicircle than those of pristine Mn and $C_{60}$, suggesting that $Mn/C_{60}$ exhibited smaller charge transfer impedance than pristine Mn and $C_{60}$, revealing that the strong electronic interactions between Mn and $C_{60}$ stemming from the built-in electric field can effectively facilitate effective charge transfer and thereby create localized electrophilic and nucleophilic regions. The created localized nucleophilic and electrophilic regions facilitated the adsorption of reactants/intermediates, thereby altering the reaction kinetics and ultimately enhancing NRR activity.[52]

So far, we have validated the role of the rationally designed built-in electric field in facilitating the adsorption of inert $N_2$, suppressing competitive *H adsorption and accelerating the reaction kinetics. However, the previously mentioned (i) limiting potentials of the HER and NRR, and (ii) how the built-in electric field reduced the energy barrier of the NRR, had not yet been discussed. To be more specific, both of them were closely related to the reaction process and pathway of the NRR. Therefore, further DFT calculations were performed to elaborate on the reaction mechanism by analyzing the variation of intermediates and the energy barriers throughout the reaction process. Both the NRR and the HER are electrochemical processes that involve the transfer of both protons and electrons, a mechanism known as proton-coupled electron transfer (PCET).[53] In the absence of Li mediation and no N atoms on the catalyst surface, the NRR mechanism can be classified into the following pathways: distal-associative pathway, alternating-associative pathway, dissociative pathway, and enzymatic pathway.[6,23,54] Among these, the dissociative pathway was difficult to achieve under mild conditions, as it required the direct cleavage of the N≡N triple bond to obtain nitrogen atoms for protonation and hydrogenation. Therefore, the feasible reaction pathways were limited to the (i) distal-associative pathway, (ii) alternating-associative pathway, and (iii) enzymatic pathway (Fig. 5g). Generally, the optimal reaction pathway could be determined by the adsorption configuration of $N_2$ and the hydrogenation order of N atoms.

As aforementioned, the adsorption of $N_2$ molecules onto the pristine $C_{60}$ surface was highly unfavorable due to the rela-

 

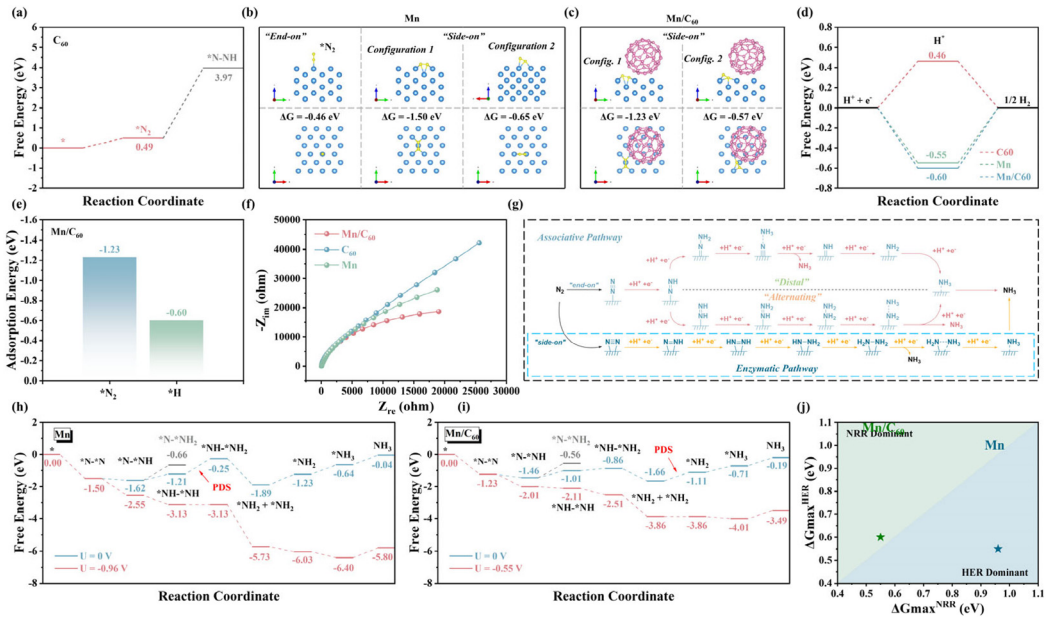


**Fig. 5** (a) The free energy of $N_2 \rightarrow *N_2H$ over $C_{60}$. (b and c) The model and results of $N_2$ adsorption energy calculations for (b) pristine Mn (101) and (c) Mn(101)/$C_{60}$ with different molecular configurations. (d) The calculated free-energy diagram of the HER for pristine $C_{60}$, pristine Mn, and Mn/$C_{60}$. (e) The computed adsorption energy of $*N_2$ and *H on Mn/$C_{60}$. (f) Nyquist plots of electrochemical impedance spectra (EIS) of Mn/$C_{60}$, $C_{60}$, and Mn. (g) Three different reaction pathways for the NRR including the distal-associative pathway, alternating-associative pathway, and enzymatic pathway. (h and i) DFT-calculated reaction pathways and the corresponding energy barriers for the NRR on pristine Mn and Mn/$C_{60}$. (j) Maximum free energies required for activating the NRR and HER on pristine Mn and Mn/$C_{60}$, where the green and blue regions indicate NRR and HER dominance, respectively.

tively high free energy barrier (Fig. 5a). Therefore, the reaction pathways for the NRR were only discussed for Mn and Mn/$C_{60}$. Fig. 5b demonstrates that, compared to the end-on configuration, $N_2$ adsorbed in a side-on configuration on pristine Mn sites exhibited a lower adsorption energy (end-on: −0.46 eV and side-on: −1.50 eV), indicating that the adsorption behavior of $N_2$ on Mn was primarily dominated by side-on adsorption. Similarly, after calculating the adsorption energies of the two $N_2$ adsorption configurations on Mn/$C_{60}$, it was found that $N_2$ was more favored to adsorb in a side-on configuration at the Mn sites on Mn/$C_{60}$, and geometrically, it tended to adopt a more energetically stable configuration, as demonstrated in Fig. 5c ($\Delta G_{*N_2}$: configuration 1, −1.23 eV; configuration 2, −0.57 eV). Therefore, the enzymatic pathway was considered the primary reaction pathway for the NRR on Mn/$C_{60}$.

The relevant reaction intermediates and NRR free energy diagrams obtained through DFT calculations are presented in Fig. 5h and i, with detailed calculation methods in the ESI.† Typically, in the enzymatic pathway, the hydrogenation steps proceeded alternately, with hydrogen atoms binding to nitrogen atoms in a sequential manner.[55] As shown in Fig. 5h and i, on both Mn and Mn/$C_{60}$, the intermediate *NH–*NH formed in the second hydrogenation step exhibited a lower free energy compared to *N–*$NH_2$ (Mn: *NH–*NH, −1.21 eV; *N–*$NH_2$, −0.66 eV; Mn/$C_{60}$: *NH–*NH, −1.01 eV; *N–*$NH_2$, −0.56 eV). Therefore, the reaction mechanism followed an alternating hydrogenation strategy, *i.e.*, the enzymatic pathway. For pristine Mn, the third hydrogenation step (*NH–*NH + $H^+$ + $e^-$ → *NH–*$NH_2$) was the potential-determining step (PDS) of the NRR, with an energy barrier of 0.96 eV. However, for Mn/$C_{60}$, the built-in electric field in the Mn/$C_{60}$ heterojunction effectively lowered the Gibbs free energy of the key intermediate *NH–*$NH_2$ from −0.25 eV to −0.86 eV and thereby reduced the free energy barrier for the potential-determining step in pristine Mn from 0.96 eV to 0.15 eV. The potential-determining step for the NRR on Mn/$C_{60}$ was confirmed to be the hydrogenation reduction of *$NH_2$–*$NH_2$ to *$NH_2$ and $NH_3$, for which a Gibbs free energy of only 0.55 eV was required to overcome the free energy barrier, demonstrating a lower energy barrier for the potential-determining step. The thermodynamic limiting potential ($U_L = -\Delta G_{PDS}/e$) was defined as the highest potential at which none of the reaction steps were uphill in free energy.[56,57] It is noteworthy that the thermodynamic limiting potential for the NRR on pristine Mn was considerably lower than that for the HER ($U_{L(NRR)}$: −0.96 V; $U_{L(HER)}$: −0.55 V). In contrast, the thermodynamic limiting potential for the NRR on Mn/$C_{60}$ ($U_{L(NRR)}$: −0.55 V) was higher than that for the HER ($U_{L(HER)}$: −0.60 V), suggesting enhanced NRR selectivity (Fig. 5j).

Combining the aforementioned experimental and theoretical calculation results, the electrochemical NRR process catalyzed by the Mn/$C_{60}$ heterostructure could be summarized in the following steps: (i) the spontaneous charge transfer at the heterointerfaces generated a built-in electric field, which then (ii) facilitated the formation of electrophilic/nucleophilic regions by electrostatic interaction. (iii) The space-charge regions enhanced the adsorption of the key intermediate *NH–

*$NH_2$, lowered the energy barrier of the NRR to −0.55 eV for the potential-determining step, improved the limiting potential of the NRR and thereby enhanced NRR activity and selectivity.

## Conclusions

In summary, we have demonstrated that the $Mn/C_{60}$ heterostructure obtained by a simple grinding and low-temperature (300 °C) annealing process showed excellent electrocatalyst activity for the electrocatalytic conversion of $N_2$ to $NH_3$ under ambient conditions. The fabricated $Mn/C_{60}$ achieved a high FE of 42.18% and a high $NH_3$ yield rate of 14.52 μg $h^{-1}$ $mg_{cat}^{-1}$ in 0.08 M $Na_2HPO_4$ solution at −0.4 V *vs.* RHE. A series of characterization techniques, electrochemical tests, and theoretical calculations suggested that the built-in electric field at the $Mn/C_{60}$ heterojunction promoted local charge redistribution, thereby endowing the $Mn/C_{60}$ surface with distinct nucleophilic and electrophilic sites that can effectively optimize the adsorption energy of the key intermediate *NH–*$NH_2$ from −0.25 eV to −0.86 eV and reduce the free energy barrier to 0.15 eV for the third hydrogenation step (*NH–*NH + $H^+$ + $e^-$ → *NH–*$NH_2$). Additionally, the NRR on $Mn/C_{60}$ exhibited a lower limiting potential (−0.55 V) compared to the HER (−0.60 V), indicating an enhancement in NRR selectivity. This study indicates that designing electrocatalysts through the design and construction of heterostructures is a promising strategy for the electrocatalytic NRR.

## Author contributions

Hao Xue: conceptualization, methodology, software, validation, formal analysis, investigation, resources, data curation, writing – original draft, writing – review & editing, and visualization. Kaiheng Zhao: XRD and SEM investigations, formal analysis, investigation, and data curation. Denglei Gao: DFT calculations, methodology, software, formal analysis, investigation, resources, data curation, and writing – review & editing. Fangying Duan: methodology, electrochemical testing, software, validation, formal analysis, investigation, resources, and data curation. Zijian Gao: methodology, electrochemical testing, software, validation, formal analysis, investigation, resources, and data curation. Wenjia Yu: methodology, electrochemical testing, software, validation, formal analysis, investigation, resources, and data curation. Sha Li: conceptualization, validation, formal analysis, investigation, resources, data curation, writing – review & editing, project administration and funding acquisition. Menglei Yuan: conceptualization, validation, resources, data curation, writing – original draft, writing – review & editing, visualization, supervision, project administration and funding acquisition. Zongjing Lu: conceptualization, validation, formal analysis, investigation, resources, data curation, writing – review & editing, supervision, project administration and funding acquisition.

## Data availability

The data supporting this article have been included as part of the ESI.†

## Conflicts of interest

There are no conflicts to declare.

## Acknowledgements

This work is supported by the National Natural Science Foundation of China (52302310), the QinChuangYuan Cites High-level Innovation and Entrepreneurship Talent Programs (QCYRCXM-2022-335), the Shanghai 2023 "Science and Technology Innovation Action Plan" Social Development Science and Technology Research Project (23DZ1203004), the Guangdong Basic and Applied Basic Research Foundation (2023A1515012816), the Fundamental Research Funds for the Central Universities (G2022KY05111), and the Open Project Program of Anhui Province International Research Center on Advanced Building Materials (JZCL2303KF).

## References

1 V. Rosca, M. Duca, M. T. de Groot and M. T. M. Koper, *Chem. Rev.*, 2009, **109**, 2209–2244.
2 Z. Wang, F. Gong, L. Zhang, R. Wang, L. Ji, Q. Liu, Y. Luo, H. Guo, Y. Li, P. Gao, X. Shi, B. Li, B. Tang and X. Sun, *Adv. Sci.*, 2019, **6**, 1801182.
3 X. Fu, V. A. Niemann, Y. Zhou, S. Li, K. Zhang, J. B. Pedersen, M. Saccoccio, S. Z. Andersen, K. Enemark-Rasmussen, P. Benedek, A. Xu, N. H. Deissler, J. B. V. Mygind, A. C. Nielander, J. Kibsgaard, P. C. K. Vesborg, J. K. Nørskov, T. F. Jaramillo and I. Chorkendorff, *Nat. Mater.*, 2024, **23**, 101–107.
4 S. Li, Y. Zhou, X. Fu, J. B. Pedersen, M. Saccoccio, S. Z. Andersen, K. Enemark-Rasmussen, P. J. Kempen, C. D. Damsgaard, A. Xu, R. Sažinas, J. B. V. Mygind, N. H. Deissler, J. Kibsgaard, P. C. K. Vesborg, J. K. Nørskov and I. Chorkendorff, *Nature*, 2024, **629**, 92–97.
5 X. Fu, J. Zhang and Y. Kang, *Chem Catal.*, 2022, **2**, 2590–2613.
6 G. Duan, Y. Chen, Y. Tang, K. A. M. Gasem, P. Wan, D. Ding and M. Fan, *Prog. Energy Combust. Sci.*, 2020, **81**, 100860.
7 M. Yuan, J. Chen, Y. Bai, Z. Liu, J. Zhang, T. Zhao, Q. Shi, S. Li, X. Wang and G. Zhang, *Chem. Sci.*, 2021, **12**, 6048–6058.
8 J. Mu, X.-W. Gao, T. Yu, L.-K. Zhao, W.-B. Luo, H. Yang, Z.-M. Liu, Z. Sun, Q.-F. Gu and F. Li, *Adv. Sci.*, 2024, **11**, 2308979.
9 N. G. Mohan and K. Ramanujam, *Curr. Opin. Electrochem.*, 2024, **45**, 101520.

 

10 H. Wang, C. Zhang, B. Liu, W. Li, C. Jiang, Z. Ke, D. He and X. Xiao, *Adv. Mater.*, 2024, **36**, 2401032.
11 Y. Wan, Z. Wang, J. Li and R. Lv, *ACS Nano*, 2022, **16**, 643–654.
12 H. Xue, Z.-H. Zhao, M. Yuan and G. Zhang, *Green Energy Environ.*, 2024, DOI: **10.1016/j.gee.2024.06.006**.
13 M. Qiao, J. Xie and D. Zhu, *Nanoscale*, 2024, **16**, 3676–3684.
14 Y. Liu, Y. Su, X. Quan, X. Fan, S. Chen, H. Yu, H. Zhao, Y. Zhang and J. Zhao, *ACS Catal.*, 2018, **8**, 1186–1191.
15 Z. Lu, H. Wang, Y. Tao, S. Zhu, W. Hao, X. Liu, Y. Min and J. Fan, *Nanoscale*, 2023, **15**, 14847–14857.
16 X. Zhao, M. Liu, Y. Wang, Y. Xiong, P. Yang, J. Qin, X. Xiong and Y. Lei, *ACS Nano*, 2022, **16**, 19959–19979.
17 M. Yuan, J. Chen, Y. Bai, Z. Liu, J. Zhang, T. Zhao, Q. Wang, S. Li, H. He and G. Zhang, *Angew. Chem., Int. Ed.*, 2021, **60**, 10910–10918.
18 M. Wang, S. Liu, T. Qian, J. Liu, J. Zhou, H. Ji, J. Xiong, J. Zhong and C. Yan, *Nat. Commun.*, 2019, **10**, 341.
19 S. Zhang, M. Jin, T. Shi, M. Han, Q. Sun, Y. Lin, Z. Ding, L. R. Zheng, G. Wang, Y. Zhang, H. Zhang and H. Zhao, *Angew. Chem., Int. Ed.*, 2020, **59**, 13423–13429.
20 H. Tao, C. Choi, L.-X. Ding, Z. Jiang, Z. Han, M. Jia, Q. Fan, Y. Gao, H. Wang, A. W. Robertson, S. Hong, Y. Jung, S. Liu and Z. Sun, *Chem*, 2019, **5**, 204–214.
21 Z. Geng, Y. Liu, X. Kong, P. Li, K. Li, Z. Liu, J. Du, M. Shu, R. Si and J. Zeng, *Adv. Mater.*, 2018, **30**, 1803498.
22 L. Han, X. Liu, J. Chen, R. Lin, H. Liu, F. Lü, S. Bak, Z. Liang, S. Zhao, E. Stavitski, J. Luo, R. R. Adzic and H. L. Xin, *Angew. Chem., Int. Ed.*, 2019, **58**, 2321–2325.
23 S. Qiang, F. Wu, J. Yu, Y.-T. Liu and B. Ding, *Angew. Chem., Int. Ed.*, 2023, **62**, e202217265.
24 M.-A. Légaré, G. Bélanger-Chabot, R. D. Dewhurst, E. Welz, I. Krummenacher, B. Engels and H. Braunschweig, *Science*, 2018, **359**, 896–900.
25 P. W. Ludden and R. H. Burris, *Science*, 1976, **194**, 424–426.
26 L. Zhang, X.-Y. Xie, H. Wang, L. Ji, Y. Zhang, H. Chen, T. Li, Y. Luo, G. Cui and X. Sun, *Chem. Commun.*, 2019, **55**, 4627–4630.
27 L. Han, M. Hou, P. Ou, H. Cheng, Z. Ren, Z. Liang, J. A. Boscoboinik, A. Hunt, I. Waluyo, S. Zhang, L. Zhuo, J. Song, X. Liu, J. Luo and H. L. Xin, *ACS Catal.*, 2021, **11**, 509–516.
28 Y. Ma, Y. Lu, C. Li, L. Hu, H. Zhang and J. Feng, *Catal. Lett.*, 2024, **154**, 5830–5837.
29 L. Zhang, L.-X. Ding, G.-F. Chen, X. Yang and H. Wang, *Angew. Chem., Int. Ed.*, 2019, **58**, 2612–2616.
30 K. Chu, Y.-p. Liu, Y.-b. Li, Y.-l. Guo, Y. Tian and H. Zhang, *Appl. Catal., B*, 2020, **264**, 118525.
31 X. Wang, D. Wu, S. Liu, J. Zhang, X.-Z. Fu and J.-L. Luo, *Nano-Micro Lett.*, 2021, **13**, 125.
32 W. Lu, T. Zheng, X. Zhang, T. He, Y. Sun, S. Li, B. Guan, D. Zhang, Z. Wei, H. Jiang, H. J. Fan and F. Du, *Angew. Chem., Int. Ed.*, 2024, e202417171.
33 S. Singla, S. Sharma, S. Basu, N. P. Shetti and T. M. Aminabhavi, *Int. J. Hydrogen Energy*, 2021, **46**, 33696–33717.
34 R. Zhang, Y. Li, X. Zhou, A. Yu, Q. Huang, T. Xu, L. Zhu, P. Peng, S. Song, L. Echegoyen and F.-F. Li, *Nat. Commun.*, 2023, **14**, 2460.
35 B. Zhao, F. Chen, C. Cheng, L. Li, C. Liu and B. Zhang, *Adv. Energy Mater.*, 2023, **13**, 2204346.
36 Y. Pan, X. Liu, W. Zhang, Z. Liu, G. Zeng, B. Shao, Q. Liang, Q. He, X. Yuan, D. Huang and M. Chen, *Appl. Catal., B*, 2020, **265**, 118579.
37 V. Martínez-Agramunt and E. Peris, *Inorg. Chem.*, 2019, **58**, 11836–11842.
38 M. Grandcolas, J. Ye and K. Miyazawa, *Ceram. Int.*, 2014, **40**, 1297–1302.
39 T. He, G. Gao, L. Kou, G. Will and A. Du, *J. Catal.*, 2017, **354**, 231–235.
40 A. R. Puente Santiago, T. He, O. Eraso, M. A. Ahsan, A. N. Nair, V. S. N. Chava, T. Zheng, S. Pilla, O. Fernandez-Delgado, A. Du, S. T. Sreenivasan and L. Echegoyen, *J. Am. Chem. Soc.*, 2020, **142**, 17923–17927.
41 M. A. Ahsan, T. He, K. Eid, A. M. Abdullah, M. L. Curry, A. Du, A. R. Puente Santiago, L. Echegoyen and J. C. Noveron, *J. Am. Chem. Soc.*, 2021, **143**, 1203–1215.
42 H. Chen, W. Zhou, D. Zhu, Z. Liu, Z. Feng, J. Li and Y. Chen, *J. Alloys Compd.*, 2020, **813**, 151812.
43 Q. Huang, W. Yang, Y. Yan, S. Xie, A. Yu, T. Xu, Y. Zhao, P. Peng and F.-F. Li, *Adv. Funct. Mater.*, 2024, 2409406.
44 A. Chourasia and D. Chopra, *Surf. Sci. Spectra*, 1994, **3**, 74–81.
45 J. Hu, A. Al-Salihy, J. Wang, X. Li, Y. Fu, Z. Li, X. Han, B. Song and P. Xu, *Adv. Sci.*, 2021, **8**, 2103314.
46 J. Wang, L. Yu, L. Hu, G. Chen, H. Xin and X. Feng, *Nat. Commun.*, 2018, **9**, 1795.
47 X. Wu, L. Xia, Y. Wang, W. Lu, Q. Liu, X. Shi and X. Sun, *Small*, 2018, **14**, 1803111.
48 K. Jia, Y. Wang, Q. Pan, B. Zhong, Y. Luo, G. Cui, X. Guo and X. Sun, *Nanoscale Adv.*, 2019, **1**, 961–964.
49 Z. Xue, C. Sun, M. Zhao, Y. Cui, Y. Qu, H. Ma, Z. Wang and Q. Jiang, *ACS Appl. Mater. Interfaces*, 2021, **13**, 59834–59842.
50 M. Liu, S. Yin, T. Ren, Y. Xu, Z. Wang, X. Li, L. Wang and H. Wang, *ACS Appl. Mater. Interfaces*, 2021, **13**, 47458–47464.
51 J. Wang, H. Jang, G. Li, M. G. Kim, Z. Wu, X. Liu and J. Cho, *Nanoscale*, 2020, **12**, 1478–1483.
52 M. Yuan, S. Dipazir, M. Wang, Y. Sun, D. Gao, Y. Bai, M. Zhang, P. Lu, H. He, X. Zhu, S. Li, Z. Liu, Z. Luo and G. Zhang, *J. Mater. Chem. A*, 2019, **7**, 3317–3326.
53 L. Hu, Z. Xing and X. Feng, *ACS Energy Lett.*, 2020, **5**, 430–436.
54 T. He, S. K. Matta and A. Du, *Phys. Chem. Chem. Phys.*, 2019, **21**, 1546–1551.
55 F. Lai, W. Zong, G. He, Y. Xu, H. Huang, B. Weng, D. Rao, J. A. Martens, J. Hofkens, I. P. Parkin and T. Liu, *Angew. Chem., Int. Ed.*, 2020, **59**, 13320–13327.
56 A. Kulkarni, S. Siahrostami, A. Patel and J. K. Nørskov, *Chem. Rev.*, 2018, **118**, 2302–2312.
57 Y. Zhang, J. Huang and M. Eikerling, *Electrochim. Acta*, 2021, **400**, 139413.